Growth in Low Carbon Conditions Reveals Amino-Acid-Coupled Iron Uptake

Juanita Lara-Gutiérrez[1]*, Jen Nguyen[1,2], Matthew R. McIlvin[3], Ichiko Sugiyama[3], Dawn M. Moran[3], Zachary Landry[1]†, Uria Alcolombri[1]‡, Johannes M. Keegstra[1], Sammy Pontrelli[4], Joaquín Jiménez-Martínez[1,5], Uwe Sauer[4], Terence Hwa[6,7], Mak A. Saito[3]*, Roman Stocker[1]*

[1] Institute for Environmental Engineering, Department of Civil, Environmental and Geomatic Engineering, ETH Zürich; Zürich, Switzerland
[2] Microbiology Graduate Program, Massachusetts Institute of Technology; Cambridge, Massachusetts, USA
[3] Marine Chemistry and Geochemistry Department, Woods Hole Oceanographic Institution; Woods Hole, Massachusetts, USA
[4] Institute of Molecular Systems Biology, Department of Biology, ETH Zürich; Zürich, Switzerland
[5] Department of Water Resources and Drinking Water, Swiss Federal Institute of Aquatic Science and Technology (Eawag); Dübendorf, Switzerland
[6] Department of Physics, U.C. San Diego; La Jolla, California, USA
[7] Division of Biological Sciences, U.C. San Diego; La Jolla, California, USA

*Corresponding authors: romanstocker@ethz.ch, msaito@whoi.edu, gutierrez@ifu.baug.ethz.ch

† Present address: Department of Marine and Environmental Biology, University of Southern California; Los Angeles, CA, USA.

‡ Present address: Department of Plant and Environmental Sciences, Institute of Life Science, The Hebrew University of Jerusalem; Jerusalem, Israel.

Abstract

Bacteria in nature encounter substrates at widely varying concentrations, yet studies of bacterial physiology have focused more on nutrient type than concentration, partly due to challenges in maintaining low concentrations. We developed a Millifluidic Continuous Culture Device (MCCD) to culture bacteria under precisely controlled nutrient conditions, including very low concentrations, in a manner suitable for proteomic analysis. Using the MCCD, we cultured *Escherichia coli* with a mixture of amino acids as the sole carbon source at three concentrations supporting growth rates spanning a fivefold range. Surprisingly, at the lowest concentration, cells exhibited proteomic signatures of iron shortage despite constant iron levels across conditions. Uptake of labeled iron-histidine and iron-cysteine complexes demonstrated that amino-acid-bound iron is bioavailable to *E. coli*. These findings reveal a previously unknown mechanism of bacterial iron acquisition that emerged under the flow imposed by the MCCD, which diluted the siderophore pool and reduced their efficacy. This work highlights the importance of studying bacterial physiology under low nutrient concentrations and demonstrates how physical conditions, such as flow, shape microbial nutrient acquisition strategies.

Main Text

Bacteria constitute one of the largest biomass fractions on the planet (*1*), contribute to host health and disease (*2*), and play essential roles in biogeochemical cycles (*3*). In environments ranging from the gut to the ocean, bacteria often encounter low concentrations of diverse nutrients that limit their growth (*4–9*). Understanding bacterial growth under nutrient-limited conditions is challenging for multiple reasons. First, mimicking such conditions in the laboratory for extended periods is difficult: although chemostats are commonly used to study low-nutrient regimes, the use of low dilution rates can lead to inhomogeneities in nutrient distribution (*10*). Second, the interplay between multiple nutrient shortages can trigger complex physiological responses: the uptake of one nutrient may rely on the availability of another, creating a dependency in nutrient acquisition.

Proteomics has emerged as a valuable approach for mechanistically understanding bacterial physiological responses to environmental change (*11–15*) and diagnosing resource shortages, as one can infer underlying stressors from observed protein abundances (*16*). While microfluidic approaches have enabled the study of bacterial physiology under low nutrient conditions (*17*), these methods typically yield insufficient biomass for proteomic analysis. Consequently, studies on bacterial physiology have primarily relied on bulk cultures with saturating nutrient concentrations and have mainly investigated how different nutrient types affect bacterial growth rates and physiological states (*12*, *18–25*). To address this limitation, we developed a novel cultivation method that allows proteomic investigation of bacterial populations grown under a broad range of nutrient concentrations.

Here, we introduce the Millifluidic Continuous Culture Device (MCCD), which enables the cultivation of bacterial populations under constant nutrient conditions. Using the MCCD, we analyzed the proteome of *Escherichia coli* grown under different concentrations of a nutrient mixture containing amino acids, nucleobases, and vitamins. Our analysis revealed broad proteomic shifts across nutrient concentrations, including a reduction in amino acid biosynthesis enzymes at higher nutrient concentrations. This finding contrasts with results from studies conducted under saturating conditions that varied only the organic carbon source.

Unexpectedly, despite varying only carbon substrate concentrations, in the low nutrient condition cells displayed a proteomic signature indicative of iron shortage. Based on these findings and on the results of a chemical equilibrium model, we propose that amino acids form complexes with iron that are bioavailable to the bacteria, so that the low abundance of amino acids in the low nutrient concentration resulted in iron limitation. This hypothesis was confirmed by uptake experiments with ^{57}Fe, demonstrating that *E. coli* can acquire iron when it is complexed with cysteine or histidine and thus revealing a previously unrecognized role for amino acids in facilitating iron uptake. Given the pervasive scarcity of iron across microbial habitats, our findings suggest that the role of free amino acids in iron uptake may be pervasive in microbial ecology.

A novel device to cultivate cells for proteomics at low nutrient concentrations

We developed the Millifluidic Continuous Culture Device (MCCD), a device that enables the cultivation of bacterial populations under approximately constant nutrient conditions, even at low concentrations, by maintaining continuous fluid flow. The MCCD supports the accumulation of sufficient bacterial biomass for proteomic analysis, providing a new approach to study bacterial physiological responses to nutrient stress. Additionally, the presence of continuous flow mimics the dynamic conditions encountered in many natural microbial habitats. The device delivers a

steady supply of fresh medium to bacterial cells growing within a Sterivex filter (Fig. 1A). The 0.45-µm pore size filter contained within a 2.5-mL cylinder (Fig. 1A, dotted inset) permits the flow of nutrients (2 mL/min) while retaining cells, facilitating biomass accumulation for downstream analyses.

We grew *E. coli* in a MOPS-based medium (*26*) with three concentrations of a rich-defined medium (RDM) supplement to impose carbon limitation and support distinct physiological states: "High" for rapid growth, "Medium" for intermediate growth, and "Low" for slow growth. The supplement, containing 20 amino acids, four nucleobases, and vitamins, was proportionally diluted across the conditions to maintain relative concentration ratios (table S1). Using the MCCD, we observed exponential growth in all conditions (fig. S1), with growth rates of 0.18 ± 0.002 h^{-1}, 0.64 ± 0.06 h^{-1}, and 0.88 ± 0.03 h^{-1} in the Low, Medium, and High conditions, respectively (Fig. 1B). The MCCD sustained exponential growth for at least three doublings in each condition. Since protein half-lives are governed by cell division (*27*), we assumed that this timescale was sufficient for the proteome to adjust to the nutrient environment.

We performed experiments and simulations to characterize the nutrient environment experienced by cells in the MCCD. Scanning electron microscopy (SEM) of the bacterial population on the filter confirmed that cells were distributed across the membrane surface in layers that were three cells thick or less when the population inside the Sterivex reached approximately 10^9 cells (Fig. 1C, fig. S2). This spatial distribution ensures minimal nutrient concentration decrease between the bottom and top layers of cells (Supplementary Text 1). Numerical simulations of the flow field in the filter revealed uniform flow velocity across the membrane surface (fig. S3A) and indicated that the pressure experienced by the bacteria due to the flowing medium was small (6.4 kPa; fig. S3B) (*28*). Finally, metabolomic analysis of the medium flowing in and out of the filters housing the bacterial population showed that, for the nutrients detectable by mass spectrometry, consumption reached up to 40% in the High condition (fig. S4), though complete nutrient exhaustion was not observed. In the Medium and Low conditions, nutrient concentrations were below the detection limit at inflow, preventing an assessment of their consumption. Together, these data indicate that the MCCD is suitable for exposing a bacterial population to approximately homogeneous and constant nutrient conditions.

Evidence of a non-carbon nutrient shortage in the Low condition despite lowest carbon concentration

To determine the relative protein abundances in *E. coli* cells cultured in each of the three nutrient concentrations, we performed liquid chromatography tandem mass spectrometry on each of four replicate samples, for each concentration. From the mass spectrometry data, we identified 1,441 proteins that account for 32% of the predicted protein-encoding genes in *E. coli* NCM3722 (Data S1, table S2). We report protein abundances as normalized spectral counts to account for variation in total spectral counts across samples, thus allowing comparison of relative protein abundances between samples. To ensure our analysis was robust to biological noise, we focused further analysis on a subset of 861 proteins that exceeded an abundance threshold (Materials and Methods). We report the abundances of these 861 proteins as percentages of total spectral counts throughout the figures and text.

To identify the biological processes with higher or lower protein abundances in each nutrient concentration as indicative of physiological responses, we used the EcoCyc database (*29*) to group the 861 proteins into functional protein groups (table S3). This analysis identified 52 functional groups, with 33 showing significant differences between nutrient concentrations ($p <$

0.05, Kruskal-Wallis test) (Fig. 2, fig. S5). We focused on these 33 functional protein groups (representing 627 proteins) for the remainder of the study. We conducted a comparative analysis of the Low and Medium conditions relative to the High condition, which was the least limiting for bacterial growth.

Hierarchical clustering of the functional protein groups revealed distinct abundance patterns across nutrient concentrations (Fig. 2). From these patterns, three main clusters emerged: protein groups that increased in abundance with higher nutrient concentration (Fig. 2, purple cluster), those that decreased (Fig. 2, green cluster), and those that peaked in the Medium concentration (Fig. 2, orange cluster). Most protein groups that increased in abundance with higher nutrient concentration (purple cluster) are associated with the demands of rapidly growing cells, such as translation, protein folding, and fatty acid biosynthesis. This cluster also included gluconeogenesis and TCA cycle enzymes, reflecting the use of amino acids as the carbon source in our experiments (*30*). Amino acids are catabolized to pyruvate and TCA cycle intermediates, which feed into the TCA cycle and gluconeogenesis pathways (*25*). The higher abundance of these enzymes indicates greater amino acid availability in this condition.

Conversely, some groups that increased in abundance with lower nutrient concentration (green cluster in Fig. 2) are part of the general stress response triggered by nutrient limitation to protect cells from stresses (*31*). These include osmoregulation, oxidative stress, and membrane integrity. Proteins in the σS regulon are known to become more abundant at slower growth rates (*22*, *31*). Our observation of increased stress response proteins in the Low and Medium conditions aligns with this, confirming that the modulation of σS levels is consistent with the slower growth rates observed in these conditions. We also observed an increase in amino acid and nucleotide biosynthesis groups with lower nutrient concentrations. This contrasts with studies of *E. coli*'s growth rate with saturating concentrations of different carbon sources, where amino acid and nucleotide biosynthesis enzymes are positively correlated with growth rate (*22*, *25*, *32*). The opposite trend in our study, where we varied carbon concentration instead, likely reflects a decreased biosynthetic requirement for amino acids and nucleotides in the Medium and High conditions, as these are provided in the culture medium.

Unexpectedly, protein groups whose relative abundance peaked in the Medium condition included those known to increase in response to carbon limitation, such as carbon catabolism (*31*, *32*), nucleotide degradation (*33–37*), and protein degradation (*38–40*) (orange cluster in Fig. 2; Fig. 3A-C). This was surprising since carbon concentrations were lowest in the Low condition, where we expected the highest abundance of these protein groups. To investigate whether this "concave expression profile" (highest abundance in the Medium condition) was present at the individual protein level, we classified each protein according to its expression profile: increasing abundance with higher nutrient concentration, increasing abundance with lower nutrient concentration, or highest abundance in the Medium concentration (see Materials and Methods and fig. S6 for classification details). Over 50% of proteins in these groups displayed the concave expression profile (Fig. 3D-F; table S4). This unexpected pattern suggests that cells in the Low condition, despite having the lowest carbon concentration, may have experienced a shortage of another nutrient.

Further support for the idea of a nutrient shortage other than carbon was observed in the abundance of enzymes involved in glycogen biosynthesis, which peaked in the Low condition ("Synthesis of storage compounds" in the green cluster in Fig. 2 and Fig. 3G-I). In *E. coli*, glycogen is synthesized when there is sufficient carbon but growth is constrained by the lack of another essential nutrient (*5*, *41*, *42*). The increased abundance of two key enzymes in the

glycogen biosynthesis pathway in the Low condition (Fig. 3H,I), especially GlgC – the first rate-limiting enzyme – suggests that the observed response in the Low condition was not solely driven by carbon scarcity.

Evidence for iron shortage in the Low condition

Our analysis revealed three lines of evidence of iron scarcity in the Low condition, based on the expression patterns of the iron acquisition protein FepA, Isc system proteins, and TCA cycle enzymes (Fig. 4A). First, FepA was 4.4 times more abundant in the Low condition compared to the Medium condition and 3.6 times more abundant than in the High condition (Fig. 4B). FepA is an outer membrane transporter induced under low-iron conditions, responsible for transporting enterobactin—a siderophore secreted by the cell to capture ferric iron with high affinity—into the periplasm (*43*, *44*). Given that the ferric uptake regulator (Fur) represses *fepA* transcription when iron concentrations are sufficient (*43*, *44*), the elevated abundance of FepA in the Low condition indicates iron availability was insufficient, triggering upregulation of this iron acquisition pathway.

Second, we found that IscU, a component of the Isc system, was least abundant in the Low condition, with a 35% decrease relative to the High condition (Fig. 4C). IscS showed a similar trend, though this was not strictly significant (Kruskal-Wallis test, $p = 0.063$, fig. S7). These observations are consistent with iron scarcity, as the Isc system, a multiprotein complex that assembles iron-sulfur clusters and transfers them to proteins for catalytic function and structural stability (Fig. 4A) (*45*), is known to be repressed under iron scarcity (*46*). In *E. coli*, downregulation of Isc proteins is part of the iron-sparing response, which conserves iron for critical functions by reducing the expression of iron-rich proteins when iron is scarce (*47*).

Third, in the Low condition we observed increased abundances of certain TCA cycle enzymes known to retain activity under iron scarcity (*48–50*). Fumarase A (FumA) and Fumarase C (FumC), which catalyze the same reaction, showed opposing expression patterns: FumA was least abundant in the Low condition, whereas FumC was most abundant (Fig. 4G,H). A similar trend was observed with the aconitase isozymes: Aconitase B (AcnB) was most abundant in the High condition, followed by the Medium condition, whereas Aconitase A (AcnA) was less abundant in the Low and Medium conditions (Fig. 4E,F). These expression patterns align with the iron dependency of these enzymes. FumC remains active under iron scarcity because, unlike FumA, it lacks an iron-sulfur cluster (*48*, *49*). Similarly, while both AcnA and AcnB have iron-sulfur clusters, AcnA is known to be more stable under low iron conditions, whereas the exposed cluster in AcnB is prone to dissociation (*50*). The concurrent upregulation of FumC and AcnA, alongside the downregulation of FumA and AcnB, reflects a signature iron-sparing response in *E. coli* (Fig. 4D) (*46*, *51*). Together, the simplest explanation for the proteome profile in the Low condition is that the cells in the Low condition experienced iron scarcity.

Iron-amino-acid complexes as bioavailable iron sources

The scarcity of iron in the Low condition is surprising, given that the same amount of iron (0.01 mM iron sulfate) and tricine (4 mM) was present in all nutrient conditions (Materials and Methods, (*26*)). We hypothesized that amino acid concentrations influenced iron availability due to the formation of iron-amino-acid complexes. The solubility of iron is strongly influenced by its redox state: ferrous iron (Fe(II)) is soluble, but in oxic environments it rapidly oxidizes to ferric iron (Fe(III)), which precipitates as nearly insoluble hydroxides (occurring at concentrations around 0.5 nM in natural waters (*52*)). However, iron can form complexes with organic compounds, including certain amino acids (*53–57*), which, when bound as Fe(II),

prevent its oxidation and maintain a soluble Fe(II) pool. In the medium we used tricine, which serves to prevent the oxidation of Fe(II) and keep it in solution (*26*). However, while tricine concentrations were constant across conditions, amino acid concentrations varied. Thus, differences in the pool of available Fe(II) complexes were likely driven by variations in amino acid concentrations.

To investigate the speciation of Fe(II), we used MINEQL+ 5.0 (*58*, *59*) to construct a chemical equilibrium model and calculate the concentrations of Fe(II) complexes in each condition. Specifically, we examined two fractions of the ferrous iron pool: Fe(II)', representing Fe(II) bound to inorganic compounds and the divalent cation species (with Fe^{2+} constituting approximately 98% of Fe(II)'; supplementary table S6), and Fe(II)L, representing Fe(II) bound to organic ligands, including iron-amino-acid complexes. The model used the concentrations of 19 amino acids (asparagine was excluded due to the lack of stability constants), tricine, and inorganic salts for each nutrient condition, based on the defined composition of the medium. Stability constants for amino acids were obtained from the MINEQL+ database (*54*, *55*). To our knowledge, stability constants for tricine have not been reported. Therefore, we substituted bicine in the model due to its structural similarity to tricine. A ligand exchange experiment confirmed comparable stability constants for bicine and tricine (Fig. S8), supporting the validity of this substitution. We set the total amount of iron as Fe(II), assuming minimal oxidation to Fe(III) based on oxidation rate estimates (Supplementary Text 2). Our results showed that Fe(II)-bicine, which accounted for the majority (95.8–98.7%) of the Fe(II) pool, and Fe(II)' remained nearly constant across the Low, Medium, and High conditions (Fig. 5A). This near-constancy indicates that tricine-bound Fe(II) and inorganic Fe(II) species were not responsible for the reduced iron availability observed in the Low condition.

In contrast, the model predicted that the Low condition had substantially lower concentrations of Fe(II) complexed with amino acids (Fig. 5A). The concentration of the Fe(II)-cysteine complex, the most abundant Fe(II)-amino-acid complex, was two orders of magnitude lower in the Low condition (0.006 μM) than in the High condition (0.297 μM). Similarly, Fe(II)-histidine and Fe(II)-serine, the next most abundant complexes, also showed concentrations two orders of magnitude lower in the Low condition compared to the High condition (Fig. 5A, table S6). Though Fe(II)' is considered to be a highly bioavailable form of iron (*60*), our proteomic and modeling data indicate that the iron shortage arose from the lower concentrations of iron-amino-acid complexes in the Low condition. Overall, our modeling results suggest that iron-amino-acid complexes serve as important bioavailable iron sources for *E. coli* and their scarcity in the Low condition led to iron scarcity.

Cysteine- and histidine-iron complexes are bioavailable iron sources for *E. coli*

To test whether iron-amino-acid complexes serve as bioavailable iron sources for *E. coli*, we conducted iron uptake experiments using the rare ^{57}Fe isotope, which constitutes only 2% of naturally occurring iron. Complexes of ^{57}Fe-Cysteine (^{57}Fe-Cys) and ^{57}Fe-Histidine (^{57}Fe-His) were prepared by mixing ^{57}Fe with cysteine or histidine at a 1:10 molar ratio and spiked into actively growing cultures in the MCCD at three timepoints, spaced 30 minutes apart. Controls included (1) a "dead cells" control with glutaraldehyde-killed cells (1.5% final concentration) spiked with the ^{57}Fe -Cys complex, (2) a non-bioavailable control with an ^{57}Fe -EDTA complex, and (3) no iron complex addition. At each timepoint, cell pellets were harvested, and intracellular iron (^{56}Fe and ^{57}Fe isotopes) concentrations were quantified using inductively coupled plasma mass spectrometry (ICP-MS).

The results showed that ^{57}Fe -amino-acid complexes were bioavailable to *E. coli*. To account for biomass differences, ^{57}Fe concentrations were normalized to phosphorus levels ([^{57}Fe]/[P]), assuming proportionality between phosphorus content and cell growth (*18*, *61*). A linear regression analysis revealed that the slopes of [^{57}Fe]/[P] for the ^{57}Fe -Cys and ^{57}Fe -His treatments were 36 and 27 μM $M^{-1}min^{-1}$, respectively. In contrast, the ^{57}Fe-EDTA and dead-cells control had slopes of 5 and 1 μM $M^{-1}min^{-1}$ (Fig. 5B). These results indicate that ^{57}Fe accumulation in the ^{57}Fe -Cys and ^{57}Fe -His treatments was active and mediated by amino acid complexation. The unchanged [^{57}Fe]/[P] levels in the dead-cell control confirmed that uptake of iron-amino-acid complexes was not passive, and the unchanged levels in the ^{57}Fe-EDTA control, acting as the non-bioavailable control, demonstrated that iron uptake was not driven by non-specific chelation.

To further examine the preferential uptake of ^{57}Fe from amino acid complexes, we compared the rates of iron uptake for ^{57}Fe, enriched with pre-formed iron-amino-acid complexes, and the most naturally abundant isotope ^{56}Fe, predominantly bound to tricine (Fig. 5A). Therefore, comparing the ratio of the uptake of the two iron isotopes reflects differences in uptake efficiency due to complexation of iron with AA. We used an ordinary least squares (OLS) linear model to analyze the time-course measurements of intracellular ^{56}Fe and ^{57}Fe concentrations for each treatment, revealing that the uptake rate of ^{57}Fe was 3.8 times higher than that of ^{56}Fe in the ^{57}Fe-Cys treatment and 5.8 times higher in the ^{57}Fe-His treatment ($p < 0.05$, two-tailed t-test, Fig. S9A,B). These results indicate that the complexation of iron with cysteine or histidine facilitates iron uptake.

Discussion

Using a novel bacterial culturing device (the MCCD), we studied the physiology of *E. coli* using proteomics in environments with different nutrient concentrations in the presence of continuous flow. In the Low condition, proteomic analysis revealed an increased abundance of siderophore-mediated iron uptake proteins and changes in iron-dependent enzymes, indicating an iron shortage. A chemical equilibrium model showed that iron-amino-acid complexes varied more than other iron species, suggesting that these complexes contribute significantly to the bioavailable iron pool. The observed iron uptake from cysteine- and histidine-bound ^{57}Fe in uptake experiments revealed that iron-amino-acid complexes are bioavailable to *E. coli*. Our findings demonstrate an unanticipated dependency of iron uptake on amino acid uptake.

Iron-amino-acid complexes may constitute a significant fraction of bioavailable iron in natural environments. Although characterized decades ago (*53–55*), their role in iron uptake has been overlooked, likely due to the prevalent use of batch cultures in physiological studies. In batch cultures, the confined environment allows for the accumulation of high-affinity organic chelators, such as siderophores, which mediate Fe(III) uptake by binding and transporting Fe(III) into the cell via specific receptors (fig. S10A) (*44*, *62*). In contrast, Fe(II) uptake occurs via diffusion across outer membrane porins and subsequent transport into the cytoplasm via the Feo system (fig. S10B) (*63*). While batch cultures enable siderophore accumulation, many natural microbial habitats are unconfined or subject to fluid flow, preventing siderophore accumulation and thus hampering this iron acquisition pathway. In our study, the continuous flow in the MCCD device acted against siderophore accumulation, allowing us to discover a role of iron-amino-acid complexes in iron uptake.

The effectiveness of iron uptake strategies is context-dependent. Siderophores, with extremely high iron binding affinity, are likely advantageous in confined or physically structured environments such as a particle, which acts as a structured island that limits diffusional loss (*64–67*). However, in unconfined environments like the open ocean, diffusional losses make siderophore use less efficient unless supported by a large population of secreting cells. It has been estimated that a cell must secrete approximately 28,000 siderophores to capture one single iron ion (*68*). Even though this can be partially mitigated by collective siderophore secretion (*68*), this imposes a significant nitrogen cost (*64*, *68*). To reduce diffusive losses, most marine bacteria use amphiphilic siderophores—siderophores with cell membrane affinity (*69*) – or employ membrane-embedded uptake systems, such as those for Fe(II), as alternative strategies for iron acquisition. The majority of soluble iron is complexed with organic ligands, categorized as "strong" (e.g., siderophores) or "weak" (e.g., amino acids) (*70*, *71*). Weak ligands, such as amino acids, are abundant, biosynthetically inexpensive, and may facilitate iron uptake with lower metabolic cost relative to siderophore production. Saccharides, another class of weak ligands, enhance iron uptake in phytoplankton (*72*). Similarly, our findings suggest that amino acids, acting as weak ligands, enable iron acquisition when taken up as metabolites by bacteria, particularly in unconfined environments where siderophores are less effective.

Iron-amino-acid complexes could be taken up either through specific transporters for these complexes or via amino acid transporters that might also allow iron hitchhiking on amino acids. Our proteomic data showed that the *E. coli* outer membrane porins OmpF and OmpC, which facilitate the transport of small molecules such as amino acids and Fe(II) into the periplasm (*63*), were most abundant in the Low condition (fig. S11). However, the observed changes in transporter abundance in our study likely resulted from the combined effects of reduced iron and amino acid availability. While specific iron-amino-acid uptake systems in bacteria have not been identified, similar transport systems have been described for other metals: both *E. coli* and *Staphylococcus aureus* possess ABC transporters that mediate the uptake of histidine-bound nickel (*73*, *74*). Future work may reveal if iron-amino-acid complexes uptake occurs through previously characterized amino acid transporters or through dedicated transporters.

We propose that the iron uptake mechanism described here plays a significant role in environments where fluid flow or diffusion limits siderophore accumulation. In humans, the gut experiences fluid flow rates of up to 20 mL/min in the small intestine (*75*) and 1.5 mL/min in the colon (*76*), which can hinder the accumulation and effectiveness of siderophores. Iron is a limiting nutrient in the gut because the majority is sequestered by high-affinity host proteins, leaving only trace amounts available to microbes (*77*). At the same time, dietary protein digestion releases peptides and free amino acids, providing a carbon and nitrogen source for gut bacteria like *E. coli* (*6*). By coupling the uptake of amino acids with iron bound to them, bacteria can acquire iron without the metabolic expense of siderophore production. Siderophores require substantial carbon and nitrogen for biosynthesis (*78*), and their loss to flow further amplifies their cost. In contrast, the uptake of iron through iron-amino acid complexes represents a more economical strategy for microbial iron acquisition in such nutrient-limited, dynamic environments.

The uptake of iron via iron-amino acid complexes is likely widespread among bacteria, as transport systems like ABC transporters are highly conserved across bacterial species (*79*). In marine environments –an unconfined environment subject to fluid flow– iron is a limiting nutrient that constrains primary productivity and bacterial heterotroph growth (*80*). Amino acids support 5–55% of bacterial nitrogen and carbon demands in these environments (*81–84*). The

SAR11 clade, for instance, assimilates up to 60% of available amino acids in oligotrophic waters (*84*), supported by high-affinity transport systems (*85*). Given the important role of amino acids as carbon and nitrogen sources, the iron uptake mechanism described here is likely broadly relevant, enabling bacteria to acquire iron through amino acid transport.

Our study revealed a striking example of iron uptake dependency on amino acid availability influenced by environmental physical conditions: fluid flow diluted the siderophore pool, making amino acids essential iron ligands for uptake and resulting in iron scarcity under low amino acid concentrations. In the absence of flow, siderophore accumulation would likely mitigate this dependency. By replicating key features of natural microbial habitats—low nutrient concentrations and fluid flow—we uncovered a previously unknown mechanism of bacterial iron uptake and demonstrated how physical conditions influence nutrient acquisition strategies.

References

1. Y. M. Bar-On, R. Phillips, R. Milo, The biomass distribution on Earth. *Proc Natl Acad Sci U S A* **115**, 6506–6511 (2018).
2. K. Hou, Z. X. Wu, X. Y. Chen, J. Q. Wang, D. Zhang, C. Xiao, D. Zhu, J. B. Koya, L. Wei, J. Li, Z. S. Chen, Microbiota in health and diseases. *Signal Transduct Target Ther* **7** (2022).
3. P. G. Falkowski, T. Fenchel, E. F. Delong, The Microbial Engines That Drive Earth's Biogeochemical Cycles. *Science (1979)* **320**, 1034–1039 (2008).
4. T. Egli, "The ecological and physiological significance of the growth of heterotrophic microorganisms with mixtures of substrates" in *Advances in Microbial Ecology* (1995)vol. 14, pp. 305–386.
5. T. Conway, P. S. Cohen, Commensal and Pathogenic Escherichia coli Metabolism in the Gut. *Microbiol Spectr* **3** (2015).
6. S. Doranga, T. Conway, K. A. Krogfelt, P. S. Cohen, Nutrition of Escherichia coli within the intestinal microbiome. *EcoSal Plus*, eesp-0006 (2024).
7. U. Muenster, Concentrations and fluxes of organic carbon substrates in the aquatic environment. *Antonie Van Leeuwenhoek* **63**, 243–274 (1993).
8. A. L. Koch, Oligotrophs versus copiotrophs. *BioEssays* **23**, 657–661 (2001).
9. C. M. Moore, M. M. Mills, K. R. Arrigo, I. Berman-Frank, L. Bopp, P. W. Boyd, E. D. Galbraith, R. J. Geider, C. Guieu, S. L. Jaccard, T. D. Jickells, J. La Roche, T. M. Lenton, N. M. Mahowald, E. Marañón, I. Marinov, J. K. Moore, T. Nakatsuka, A. Oschlies, M. A. Saito, T. F. Thingstad, A. Tsuda, O. Ulloa, Processes and patterns of oceanic nutrient limitation. *Nat Geosci* **6**, 701–710 (2013).
10. G. S. Hansford, A. E. Humphrey, The effect of equipment scale and degree of mixing on continuous fermentation yield at low dilution rates. *Biotechnol Bioeng* **8**, 85–96 (1966).
11. M. S. Guo, C. A. Gross, Stress-induced remodeling of the bacterial proteome. *Current Biology* **24**, R424–R434 (2014).
12. A. Schmidt, K. Kochanowski, S. Vedelaar, E. Ahrné, B. Volkmer, L. Callipo, K. Knoops, M. Bauer, R. Aebersold, M. Heinemann, The quantitative and condition-dependent Escherichia coli proteome. *Nat Biotechnol* **34**, 104–110 (2016).
13. A. Mateus, J. Hevler, J. Bobonis, N. Kurzawa, M. Shah, K. Mitosch, C. V. Goemans, D. Helm, F. Stein, A. Typas, M. M. Savitski, The functional proteome landscape of Escherichia coli. *Nature* **588**, 473–478 (2020).
14. C. Wu, M. Mori, M. Abele, A. Banaei-Esfahani, Z. Zhang, H. Okano, R. Aebersold, C. Ludwig, T. Hwa, Enzyme expression kinetics by Escherichia coli during transition from rich to minimal media depends on proteome reserves. *Nat Microbiol* **8**, 347–359 (2023).
15. M. Mori, S. Schink, D. W. Erickson, U. Gerland, T. Hwa, Quantifying the benefit of a proteome reserve in fluctuating environments. *Nat Commun* **8**, 1225 (2017).
16. N. G. Walworth, M. A. Saito, M. D. Lee, M. R. McIlvin, D. M. Moran, R. M. Kellogg, F. X. Fu, D. A. Hutchins, E. A. Webb, Why Environmental Biomarkers Work: Transcriptome–Proteome Correlations and Modeling of Multistressor Experiments in the Marine Bacterium Trichodesmium. *J Proteome Res* **21**, 77–89 (2022).

17. J. Nguyen, V. Fernandez, S. Pontrelli, U. Sauer, M. Ackermann, R. Stocker, A distinct growth physiology enhances bacterial growth under rapid nutrient fluctuations. *Nat Commun* **12** (2021).
18. M. Schaechter, O. Maaloe, N. O. Kjeldgaard, Dependency on Medium and Temperature of Cel Size and Chemical Composition during Balanced Growth of Salmonella typhimurium. *Microbiology (N Y)* **19**, 592–606 (1958).
19. F. C. Neidhardt, B. Magasanik, Studies on the role of ribonucleic acid in the growth of bacteria. *Biochim Biophys Acta* **42**, 99–116 (1960).
20. M. Scott, C. W. Gunderson, E. M. Mateescu, Z. Zhang, T. Hwa, Interdependence of cell growth and gene expression: origins and consequences. *Science (1979)* **330**, 1099–1102 (2010).
21. M. U. Caglar, J. R. Houser, C. S. Barnhart, D. R. Boutz, S. M. Carroll, A. Dasgupta, W. F. Lenoir, B. L. Smith, V. Sridhara, D. K. Sydykova, D. Vander Wood, C. J. Marx, E. M. Marcotte, J. E. Barrick, C. O. Wilke, The E. coli molecular phenotype under different growth conditions. *Sci Rep* **7** (2017).
22. M. Mori, Z. Zhang, A. Banaei-Esfahani, J. Lalanne, H. Okano, B. C. Collins, A. Schmidt, O. T. Schubert, D. Lee, G. Li, R. Aebersold, T. Hwa, C. Ludwig, From coarse to fine: the absolute Escherichia coli proteome under diverse growth conditions . *Mol Syst Biol* **17** (2021).
23. C. You, H. Okano, S. Hui, Z. Zhang, M. Kim, C. W. Gunderson, Y. P. Wang, P. Lenz, D. Yan, T. Hwa, Coordination of bacterial proteome with metabolism by cyclic AMP signalling. *Nature* **500**, 301–306 (2013).
24. Z. Li, M. Nimtz, U. Rinas, The metabolic potential of Escherichia coli BL21 in defined and rich medium. *Microb Cell Fact* **13** (2014).
25. S. Hui, J. M. Silverman, S. S. Chen, D. W. Erickson, M. Basan, J. Wang, T. Hwa, J. R. Williamson, Quantitative proteomic analysis reveals a simple strategy of global resource allocation in bacteria. *Mol Syst Biol* **11** (2015).
26. F. C. Neidhardt, P. L. Bloch, D. F. Smith, Culture Medium for Enterobacteria. *J Bacteriol* **119**, 736–747 (1974).
27. M. Shamir, Y. Bar-On, R. Phillips, R. Milo, SnapShot: Timescales in Cell Biology. *Cell* **164**, 1302–1302 (2016).
28. A. Guyet, M. Dade-Robertson, A. Wipat, J. Casement, W. Smith, H. Mitrani, M. Zhang, Mild hydrostatic pressure triggers oxidative responses in Escherichia coli. *PLoS One* **13** (2018).
29. I. M. Keseler, S. Gama-Castro, A. Mackie, R. Billington, C. Bonavides-Martínez, R. Caspi, A. Kothari, M. Krummenacker, P. E. Midford, L. Muñiz-Rascado, W. K. Ong, S. Paley, A. Santos-Zavaleta, P. Subhraveti, V. H. Tierrafría, A. J. Wolfe, J. Collado-Vides, I. T. Paulsen, P. D. Karp, The EcoCyc Database in 2021. *Front Microbiol* **12** (2021).
30. L. Reitzer, Catabolism of Amino Acids and Related Compounds. *EcoSal Plus* **1** (2005).
31. R. Hengge, Stationary-Phase Gene Regulation in Escherichia coli §. *EcoSal Plus* **4**, 10–1128 (2011).
32. M. Scott, T. Hwa, Shaping bacterial gene expression by physiological and proteome allocation constraints. *Nat Rev Microbiol* **21**, 327–342 (2022).
33. Y. E. Zhang, R. L. Bærentsen, T. Fuhrer, U. Sauer, K. Gerdes, D. E. Brodersen, (p)ppGpp Regulates a Bacterial Nucleosidase by an Allosteric Two-Domain Switch. *Mol Cell* **74**, 1239-1249.e4 (2019).
34. K. Nath, A. L. Koch, Protein Degradation in Escherichia coli. *Journal of Biological Chemistry* **246**, 6956–6967 (1971).
35. K. F. Jensen, G. Dandanell, B. Hove-Jensen, M. Willemoës, Nucleotides, Nucleosides, and Nucleobases. *EcoSal Plus* **3** (2008).
36. R. Kaplan, L. Cohen, E. Yagil, Acid-Soluble Degradation Products of Ribonucleic Acid in Escherichia coli and the Role of Nucleotidases in Their Catabolism. *J Bacteriol* **124**, 1159–1164 (1975).
37. L. Cohen, R. Kaplan, Accumulation of Nucleotides by Starved Escherichia coli Cells as a Probe for the Involvement of Ribonucleases in Ribonucleic Acid Degradation. *J Bacteriol* **129**, 651–657 (1977).
38. D. Weichart, N. Querfurth, M. Dreger, R. Hengge-Aronis, Global role for ClpP-containing proteases in stationary-phase adaptation of Escherichia coli. *J Bacteriol* **185**, 115–125 (2003).
39. C. A. Reeve, A. T. Bockman, A. Matin, Role of Protein Degradation in the Survival of Carbon-Starved Escherichia coli and Salmonella typhimurium. *J Bacteriol* **157**, 758–763 (1984).
40. D. Pletzer, T. M. Blimkie, H. Wolfmeier, Y. Li, A. Baghela, A. H. Y Lee, R. Falsafi, R. E. W Hancock, C. D. Pletzer, L. Ahy, H. Rew, The Stringent Stress Response Controls Proteases and

Global Regulators under Optimal Growth Conditions in Pseudomonas aeruginosa. *mSystems* **5**, 10–1128 (2020).
41. J. Preiss, T. Romeo, Molecular Biology and Regulatory Aspects of Glycogen Biosynthesis in Bacteria. *Prog Nucleic Acid Res Mol Biol* **47**, 299–329 (1994).
42. S. A. Jones, M. Jorgensen, F. Z. Chowdhury, R. Rodgers, J. Hartline, M. P. Leatham, C. Struve, K. A. Krogfelt, P. S. Cohen, T. Conway, Glycogen and maltose utilization by Escherichia coli O157:H7 in the mouse intestine. *Infect Immun* **76**, 2531–2540 (2008).
43. M. Sandy, A. Butler, Microbial iron acquisition: Marine and terrestrial siderophores. *Chem Rev* **109**, 4580–4595 (2009).
44. S. C. Andrews, A. K. Robinson, F. Rodríguez-Quiñones, Bacterial iron homeostasis. *FEMS Microbiol Rev* **27**, 215–237 (2003).
45. J. A. Imlay, The molecular mechanisms and physiological consequences of oxidative stress: Lessons from a model bacterium. *Nat Rev Microbiol* **11**, 443–454 (2013).
46. E. Massé, M. Arguin, Ironing out the problem: New mechanisms of iron homeostasis. *Trends Biochem Sci* **30**, 462–468 (2005).
47. A. Gaballa, H. Antelmann, C. Aguilar, S. K. Khakh, K.-B. Song, G. T. Smaldone, J. D. Helmann, The Bacillus subtilis iron-sparing response is mediated by a Fur-regulated small RNA and three small, basic proteins. *Proceedings of the National Academy of Sciences* **105**, 11927–11932 (2008).
48. D. H. Flint, M. H. Emptage, J. R. Guest, Fumarase A from Escherichia coli: Purification and Characterization as an Iron-Sulfur Cluster Containing Enzyme. *Biochemistry* **31**, 10331–10337 (1992).
49. S. I. Liochev, I. Fridovich, FumaraseC, the stable fumarase of Escherichia coli, is controlled by the soxRS regulon. *Proceedings of the National Academy of Sciences* **89**, 5892–5896 (1992).
50. S. Varghese, Y. Tang, J. A. Imlay, Contrasting sensitivities of Escherichia coli aconitases A and B to oxidation and iron depletion. *J Bacteriol* **185**, 221–230 (2003).
51. E. Massé, S. Gottesman, A small RNA regulates the expression of genes involved in iron metabolism in Escherichia coli. *Proceedings of the National Academy of Sciences* **99**, 4620–4625 (2002).
52. K. Kuma, J. Nishioka, K. Matsunaga, Controls on iron(III) hydroxide solubility in seawater: The influence of pH and natural organic chelators. *Limnol Oceanogr* **41**, 396–407 (1996).
53. D. B. Sabine, Metallo-Amino Acid Complexes III. iron Complexes. *Microchemical Journal* **24**, 475–478 (1979).
54. A. E. Martell, R. M. Smith, *Critical Stability Constants: Vol. 1 Amino Acids* (Plenum Press, New York, 1974)vol. 1.
55. L. G. Sillén, A. E. Martell, *Stability of Metal-Ion Complexes. Special Pub. No. 25* (The Chemical Society, London, 1971).
56. K. Severin, R. Bergs, W. Beck, Bioorganometallic chemistry-transition metal complexes with α-amino acids and peptides. *Angewandte Chemie* **37**, 1634–1654 (1998).
57. B. W. Fitzsimmons, A. Hume, L. F. Larkworthy, M. H. Turnbull, A. Yavari, The Preparation and Characterisation of Some Complexes of Iron(II) with Amino Acids. *Inorganica Chim Acta* **106**, 109–114 (1985).
58. J. C. Westall, J. L. Zachary, F. M. M. Morel, "MINEQL: A computer program for the calculation of chemical equilibrium composition of aqueous systems" (Cambridge, 1976).
59. W. D. Schecher, D. McAvoy, MINEQL+: A Chemical Equilibrium Modeling System. Environmental Research Software 5.0 [Preprint] (1998).
60. F. M. M. Morel, A. B. Kustka, Y. Shaked, The role of unchelated Fe in the iron nutrition of phytoplankton. *Limnol Oceanogr* **53**, 400–404 (2008).
61. J. B. Cotner, W. Makino, B. A. Biddanda, Temperature affects stoichiometry and biochemical composition of Escherichia coli. *Microb Ecol* **52**, 26–33 (2006).
62. K. G. Wooldridge, P. H. Williams, Iron uptake mechanisms of pathogenic bacteria. *FEMS Microbiol Rev* **12**, 325–348 (1993).
63. C. K. Y. Lau, K. D. Krewulak, H. J. Vogel, Bacterial ferrous iron transport: The Feo system. *FEMS Microbiol Rev* **40**, 273–298 (2016).
64. C. Völker, D. A. Wolf-Gladrow, A. Gladrow, Physical limits on iron uptake mediated by siderophores or surface reductases. *Mar Chem* **65**, 227–244 (1999).
65. J. Kramer, Ö. Özkaya, R. Kümmerli, Bacterial siderophores in community and host interactions. *Nat Rev Microbiol* **18**, 152–163 (2020).

66. O. X. Cordero, L. A. Ventouras, E. F. DeLong, M. F. Polz, Public good dynamics drive evolution of iron acquisition strategies in natural bacterioplankton populations. *Proceedings of the National Academy of Sciences* **109**, 20059–20064 (2012).
67. R. Kümmerli, A. S. Griffin, S. A. West, A. Buckling, F. Harrison, Viscous medium promotes cooperation in the pathogenic bacterium Pseudomonas aeruginosa. *Proceedings of the Royal Society B: Biological Sciences* **276**, 3531–3538 (2009).
68. G. E. Leventhal, M. Ackermann, K. T. Schiessl, Why microbes secrete molecules to modify their environment: The case of iron-chelating siderophores. *J R Soc Interface* **16** (2019).
69. R. M. Boiteau, D. R. Mende, N. J. Hawco, M. R. McIlvin, J. N. Fitzsimmons, M. A. Saito, P. N. Sedwick, E. F. Delong, D. J. Repeta, Siderophore-based microbial adaptations to iron scarcity across the eastern Pacific Ocean. *Proceedings of the National Academy of Sciences* **113**, 14237–14242 (2016).
70. E. L. Rue, K. W. Bruland, Complexation of iron(III) by natural organic ligands in the Central North Pacific as determined by a new competitive ligand equilibration/adsorptive cathodic stripping voltammetric method. *Mar Chem* **50**, 117–138 (1995).
71. P. W. Boyd, M. J. Ellwood, The biogeochemical cycle of iron in the ocean. *Nat Geosci* **3**, 675–682 (2010).
72. C. S. Hassler, V. Schoemann, C. M. Nichols, E. C. V. Butler, P. W. Boyd, Saccharides enhance iron bioavailability to southern ocean phytoplankton. *Proceedings of the National Academy of Sciences* **108**, 1076–1081 (2011).
73. P. T. Chivers, E. L. Benanti, V. Heil-Chapdelaine, J. S. Iwig, J. L. Rowe, Identification of Ni-(l-His)2 as a substrate for NikABCDE-dependent nickel uptake in Escherichia coli. *Metallomics* **4**, 1043–1050 (2012).
74. H. Lebrette, E. Borezée-Durant, L. Martin, P. Richaud, E. Boeri Erba, C. Cavazza, Novel insights into nickel import in Staphylococcus aureus: The positive role of free histidine and structural characterization of a new thiazolidine-type nickel chelator. *Metallomics* **7**, 613–621 (2015).
75. K. D. Fine, C. A. S. Ana, J. L. Porter, J. S. Fordtran, Effect of changing intestinal flow rate on a measurement of intestinal permeability. *Gastroenterology* **108**, 983–989 (1995).
76. J. Cremer, M. Arnoldini, T. Hwa, Effect of water flow and chemical environment on microbiota growth and composition in the human colon. *Proc Natl Acad Sci U S A* **114**, 6438–6443 (2017).
77. Y. Seyoum, K. Baye, C. Humblot, Iron homeostasis in host and gut bacteria–a complex interrelationship. *Gut Microbes* **13**, 1–19 (2021).
78. D. J. Sexton, M. Schuster, Nutrient limitation determines the fitness of cheaters in bacterial siderophore cooperation. *Nat Commun* **8** (2017).
79. A. E. Shea, V. S. Forsyth, J. A. Stocki, T. J. Mitchell, A. E. Frick-Cheng, S. N. Smith, S. L. Hardy, H. L. T. Mobley, Emerging roles for ABC transporters as virulence factors in uropathogenic Escherichia coli. *Proc Natl Acad Sci U S A* **121** (2024).
80. A. Tagliabue, A. R. Bowie, P. W. Boyd, K. N. Buck, K. S. Johnson, M. A. Saito, The integral role of iron in ocean biogeochemistry. *Nature* **543**, 51–59 (2017).
81. R. G. Keil, D. L. Kirchman, Utilization of dissolved protein and amino acids in the northern Sargasso Sea. *Aquatic Microbial Ecology* **18**, 293–300 (1999).
82. D. L. Kirchman, "The Contribution of Monomers and Other Low-Molecular Weight Compounds to the Flux of Dissolved Organic Material in Aquatic Ecosystems" in *Aquatic Ecosystems* (Academic Press, 2003).
83. R. G. Keil, D. L. Kirchman, Dissolved combined amino acids: Chemical form and utilization by marine bacteria. *Limnol Oceanogr* **38**, 1256–1270 (1993).
84. R. R. Malmstrom, R. P. Kiene, M. T. Cottrell, D. L. Kirchman, Contribution of SAR11 bacteria to dissolved dimethylsulfoniopropionate and amino acid uptake in the North Atlantic Ocean. *Appl Environ Microbiol* **70**, 4129–4135 (2004).
85. B. E. Clifton, U. Alcolombri, G. I. Uechi, C. J. Jackson, P. Laurino, The ultra-high affinity transport proteins of ubiquitous marine bacteria. *Nature*, doi: 10.1038/s41586-024-07924-w (2024).

Acknowledgments: We thank Martin Ackermann, Julia Vorholt, current and former members of the Stocker group, and members of the PriME collaboration for their helpful discussions. We are grateful to Suckjoon Jun for generously providing the NCM3722 strain of *E. coli* used in this study. We thank Miriam Lucas from ScopeM for processing samples for SEM and acquiring SEM images, as well as ScopeM for their support and technical assistance. We also thank Russell Naisbit for his critical reading, which greatly improved this manuscript, and acknowledge the use of ChatGPT-4o for grammar correction and phrasing enhancements.

Funding:

Gordon and Betty Moore Foundation Symbiosis in Aquatic Systems Initiative Investigator Award GBMF9197 (RS)

Simons Foundation through the Principles of Microbial Ecosystems (PriME) collaboration grant 542395FY22 (RS, TH)

Swiss National Science Foundation grant 205321_207488 (RS)

NSF Postdoctoral Research Fellowships in Biology Program for support under Grant No.2109890 (JN)

Author contributions:

Conceptualization: JLG, RS, MS, JN

Methodology: JLG, RS, MS, JN, UA, ZL

Investigation: JLG, MRM, IS, DMM, SP, JJM

Visualization: JLG, IS, JJM

Funding acquisition: RS, MS

Project administration: JLG

Supervision: RS, MS

Writing – original draft: JLG

Writing – review & editing: JLG, JN, JMK, UA, TH, MS, RS, and all other co-authors

Competing interests: Authors declare that they have no competing interests.

Data and materials availability: All data and code will be available upon publication.

Supplementary Materials

Materials and Methods

Supplementary Text S1 to S2

Figs. S1 to S10

Tables S1 to S6

References 316928 C9h13NO3

Data S1

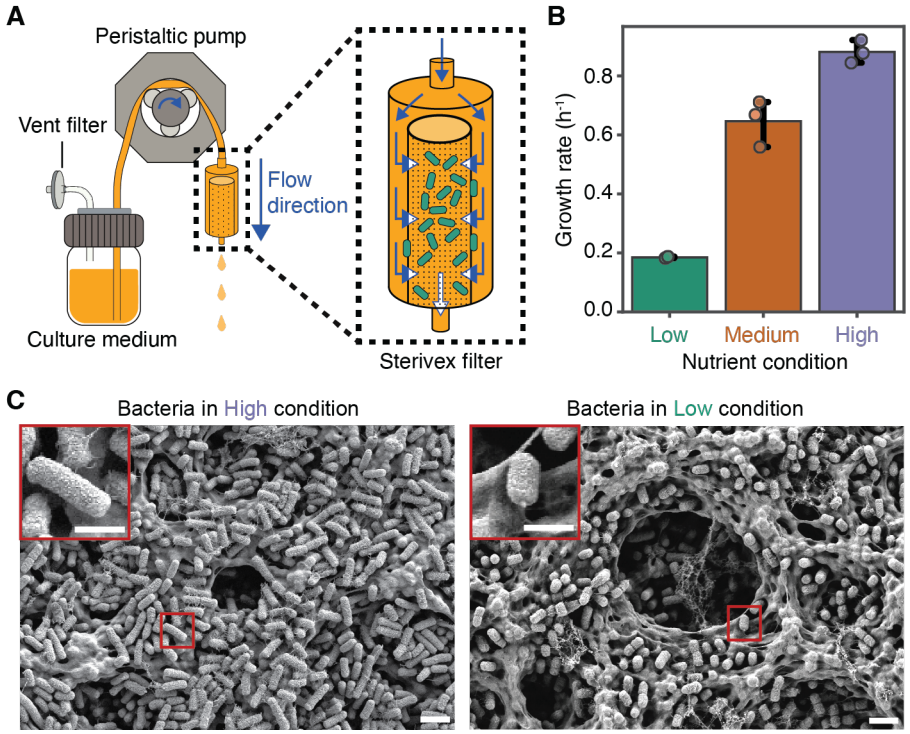

Figure 1. The Millifluidic Continuous Culture Device (MCCD) enables bacterial growth at controlled nutrient concentrations with sufficient biomass accumulation for proteomic analysis. (**A**) Schematic of the MCCD, with a magnified view of the Sterivex filter in which *E. coli* (green) are cultured. A peristaltic pump pushes sterile fresh culture medium at a set flow rate into the Sterivex filter through the inlet (top). A 0.45-µm pore size membrane (dotted shape) separates the filter inlet from the outlet (bottom), keeping cells in the filter while allowing culture medium to flow through. The medium flows into the filter (solid blue arrows) and traverses the membrane (white arrows with a blue outline), which restricts passage to the outlet, allowing only the medium to pass through while retaining bacteria, since these are larger than the pore size. (**B**) Specific growth rate of *E. coli* based on cell counts cultivated in the MCCD under Low ($n = 2$), Medium ($n = 3$), and High ($n = 3$) concentrations of rich-defined medium (RDM). Each point represents one biological replicate (n). The bar height represents the mean and error bars indicate the 95% confidence interval. The Low, Medium, and High conditions are represented by the colors green, orange, and purple, respectively. (**C**) Scanning electron microscopy (SEM) images of *E. coli* after 5 and 12 hours of growth in the High and Low conditions, respectively. The red insets show magnified views of representative bacteria. Scale bars: 2 µm (main view) and 1 µm (magnified view).

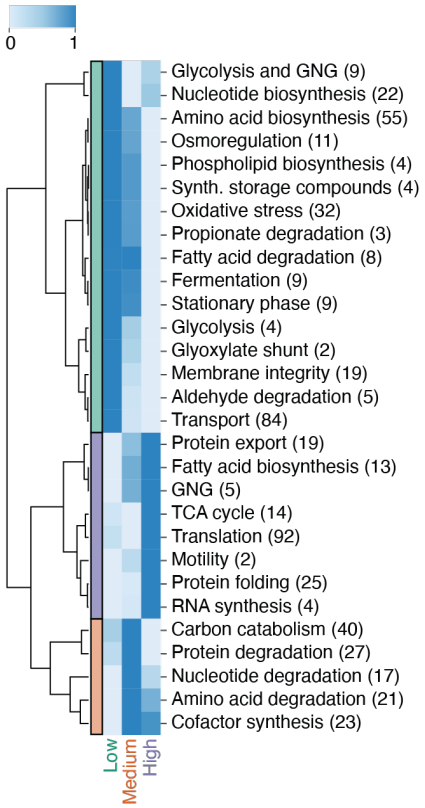

Figure 2. Protein expression profiles of functional groups under the three nutrient conditions. After hierarchical clustering, three groups of protein expression profiles emerged, depending on whether the highest protein abundance occurred in the Low (green bar), Medium (orange bar), or High (purple bar) nutrient conditions. Each row in the blue-shaded heatmap represents a biological function, encompassing proteins that contribute to that function. For each row, the following steps were applied: (1) the abundances of all proteins in the biological function group were summed for each nutrient condition, (2) the median value across four biological replicates within each nutrient condition was calculated, and (3) the median values were scaled across the row to range between 0 (lightest blue, lowest value) and 1 (darkest blue, highest value). Protein groups included in the heatmap met two criteria: they showed statistically significant differences across conditions ($p < 0.05$, Kruskal-Wallis test) and contained at least two proteins. Numbers in parentheses indicate the number of proteins in each group. See Fig. S5 for the complete heatmap.

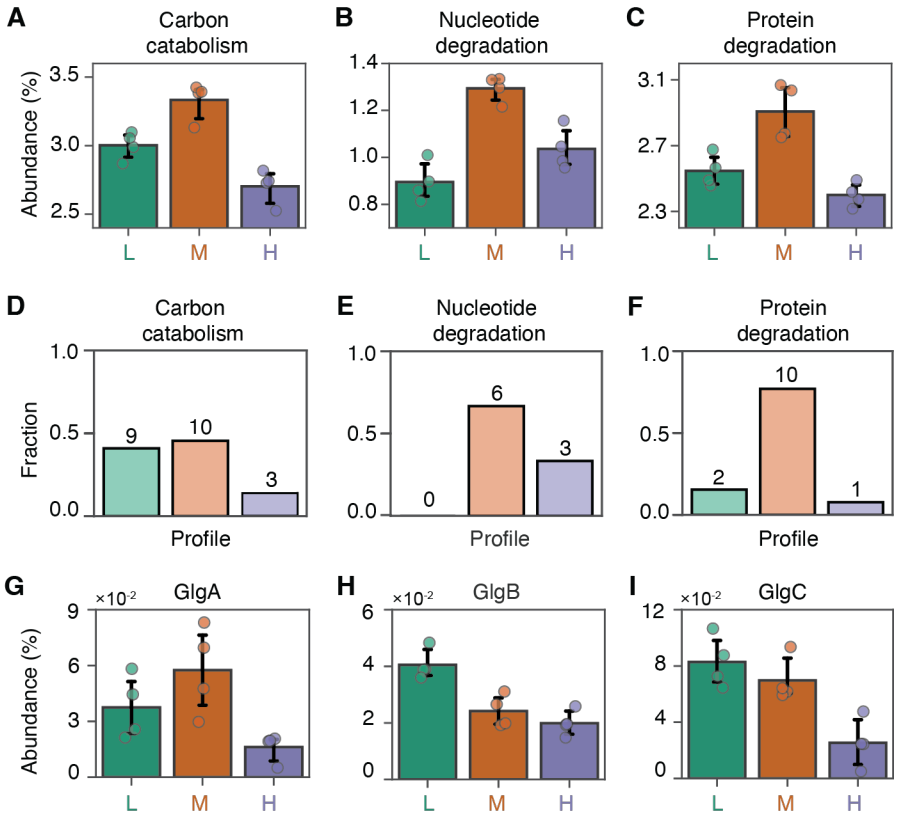

Figure 3. Protein expression suggests that carbon limits growth in the Medium condition but not in the Low condition. (**A-C**) Summed abundances of (**A**) all proteins assigned to carbon catabolism (40 proteins), (**B**) nucleotide degradation (17 proteins) and **(C)** protein degradation (27 proteins)**.** For each functional group, protein abundances were summed, including proteins with and without statistically significant changes across conditions. The bar height denotes mean value, circles represent biological replicates, and error bars indicate the 95% confidence interval. Abundance is shown as the percentage of all summed spectral counts. (**D-F**) Fraction of proteins within each functional group assigned to the protein expression profiles identified in Fig. 2: highest abundance in Low (pastel green), highest abundance in Medium (pastel orange), and highest abundance in High (pastel purple). The bar height represents the fraction of proteins from that functional group displaying each expression profile, with the number above each bar indicating the number of proteins displaying that profile. Only proteins with significant differences across conditions ($p < 0.05$, Kruskal-Wallis test) were included. (**G-I**) Abundances of glycogen biosynthesis enzymes across nutrient conditions. The bar height denotes mean value, circles represent biological replicates, and error bars indicate the 95% confidence interval. (**A-C, G-I**) Data from Low, Medium, and High nutrient conditions are represented by green, orange, and purple colors, respectively.

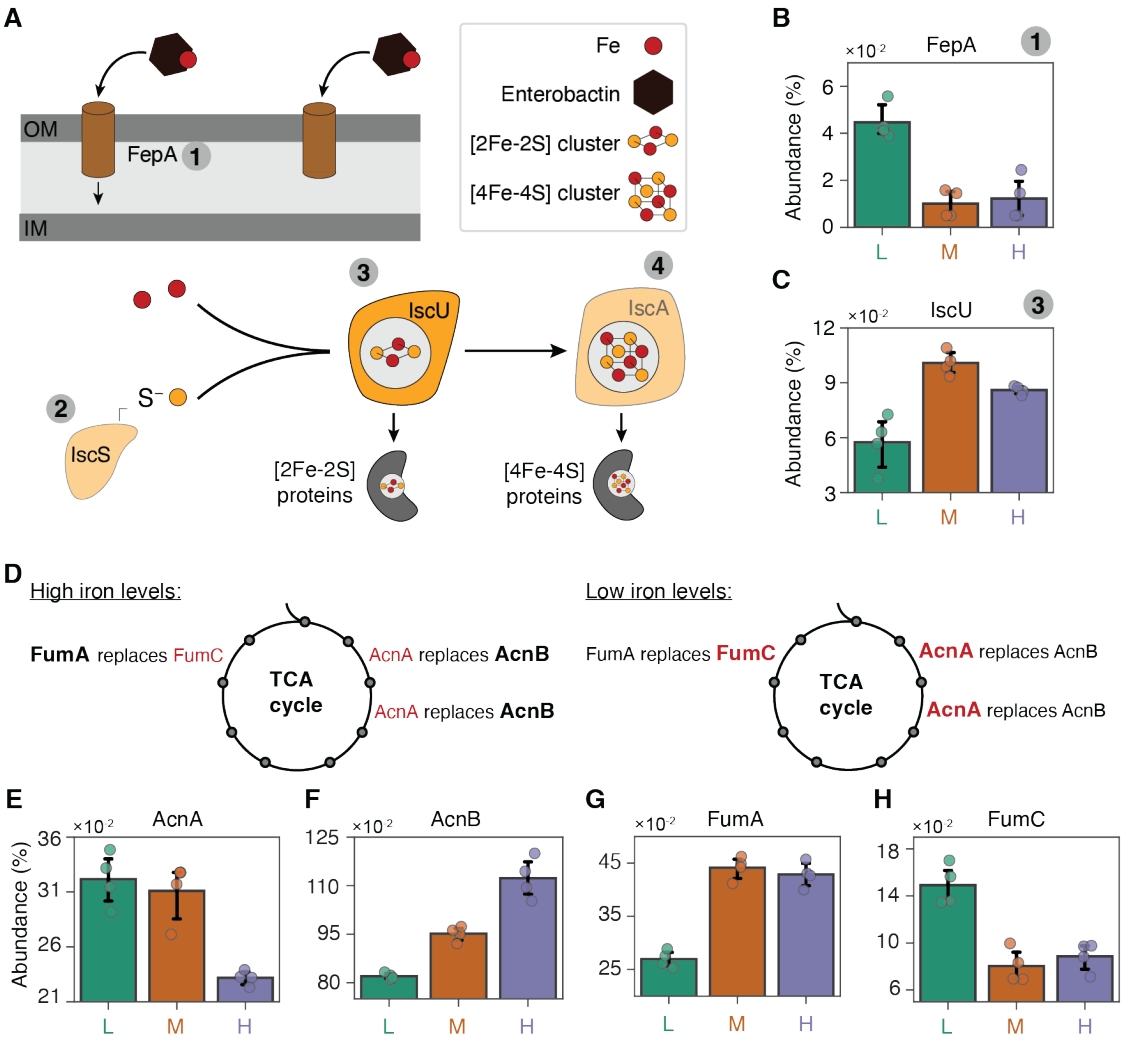

Figure 4. Evidence that iron, not carbon, was the limiting nutrient in the Low condition. (**A**) Schematic of the ferric enterobactin uptake system in *E. coli* and the use of intracellular iron by the Isc system. The transporter FepA (brown outer membrane protein) binds Fe(III)-enterobactin complexes and transports them into the periplasm. In the cytoplasm, iron is used by the Isc system to assemble iron-sulfur clusters (yellow and red networks), which are essential for the catalytic activity of client proteins receiving the clusters. Iron bound to enterobactin is Fe(III), while all other red dots symbols of Fe can be Fe(II) or Fe(III). (**B-C**) Barplots of the protein abundances of the ferric enterobactin transporter and the IscU system protein IscU across nutrient conditions. (**D**) Schematic of TCA cycle enzymes in *E. coli*, highlighting aconitases (AcnA, AcnB) and fumarases (FumA, FumC), which vary in protein abundance with intracellular iron levels. Enzymes in black lose catalytic activity when iron is low, while their isozymes in red preserve catalytic activity in low iron. Bold letters indicate the enzymes whose abundance increases in response to the specific iron condition (underlined). (**E-H**) Barplots of the protein abundances of the four TCA cycle iron-dependent enzymes across nutrient conditions. All barplots show individual protein abundances for each replicate (circles), along with the mean (bar height) and the 95% confidence interval (error bars). All the proteins shown in this figure displayed significant differences across conditions ($p < 0.05$, Kruskal-Wallis test).

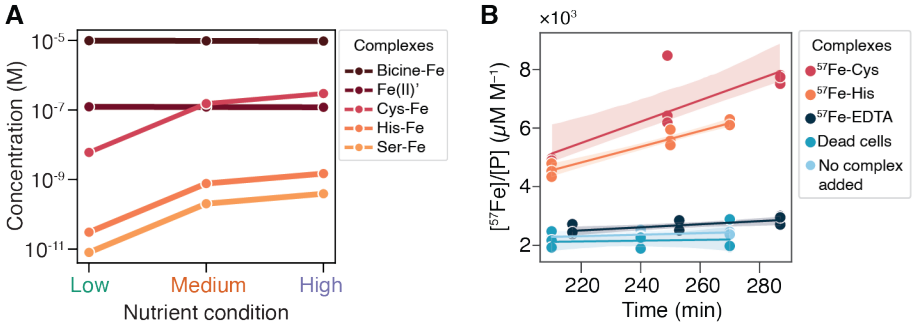

Figure 5. Iron uptake by *E. coli* via complexation with cysteine or histidine. (**A**) Fe(II) modeled in MINEQL yielded the concentrations of complexes between Fe(II) and components in the growth medium. Only the three highest concentration amino-acid-Fe(II) complexes are shown. Fe(II)' represents the sum of inorganic species including Fe^{2+}. (**B**) Time course of iron uptake, where tracer ^{57}Fe in biomass was normalized to phosphorus ([^{57}Fe]/[P]). ^{57}Fe was added as complexes with cysteine, histidine, or EDTA (low bioavailability control). Glutaraldehyde-killed cells were used as a "dead cells" control, to which the ^{57}Fe-Cys complex was added. Samples were collected at three timepoints over 90 minutes, with the first complex added at 210 min after growth initiation in the MCCD. Linear regression analysis yielded slopes of 36 and 27 μM $M^{-1}min^{-1}$ for the ^{57}Fe-Cys and ^{57}Fe-His treatments, respectively. For the controls, the slopes were 5 and 1 μM $M^{-1}min^{-1}$ for the ^{57}Fe-EDTA and dead cells controls, respectively. The shaded region indicates the 95% confidence interval of the regression estimate.